

# Exploration of the Physics of Hub Drag

Vrishank Raghav<sup>\*</sup>, Rajiv Shenoy<sup>†</sup>, Felipe T. Ortega<sup>‡</sup>

Narayanan Komerath<sup>‡</sup> and Marilyn Smith<sup>§</sup>

*School of Aerospace Engineering, Georgia Institute of Technology, Atlanta, Georgia, 30332*

Main rotor hubs contribute significantly to the helicopter's parasite drag. Due to the complex geometry of typical hub configurations, large uncertainties in loads and wake flowfield phenomena inhibit the development of improved concepts at the design stage. Experimental and computational evaluations of the near wake of a generic, subscale complex rotor hub are explored. Prior efforts have shown that state of the art computational fluid dynamics (CFD) simulations are accurate enough to predict drag characteristics of the complex hub. Velocity profiles and turbulence spectra measurements in the hub near wake (0.5 - 1.0 hub diameters) correlate well with CFD when proper fidelity of grid, time step, and turbulence model are chosen. The wake spectral content is characterized by broadband turbulence in addition to large scale spectral content energizing the flowfield. Current results substantiate earlier findings of the role played by Magnus effect due to bodies of rotation in forward flight.

## I. Introduction

Recent rotorcraft design has focused on the achievement of higher forward flight speeds, and a major obstacle the designers must overcome is the limitation of parasite drag on forward flight performance.<sup>1,2</sup> A reduction of parasite drag will increase the vehicle's range, maximum speed and payload. In general, reduction of parasite drag has been shown to improve the vehicle stability and control,<sup>3</sup> and even decrease vibrational excitation and blade loads significantly, resulting in weight reduction and blade life extension.<sup>4</sup> Parasite drag contributors for rotorcraft include the fuselage, main rotor pylon and hub, all protuberances such as landing gear and antennae, and engine protrusions. The hubs of single main rotor helicopters have been found to contribute approximately 25%-30% of the vehicle parasite drag, while coaxial hubs yield as much as 50%, as is the case with the XH-59.<sup>5</sup> To facilitate better hub designs with considerable reductions in drag, the sources of drag and physics behind the phenomena must be better understood, modeled and predicted. Hub drag requires further investigation as it is a major contributor to parasite drag.

The complex flow over a helicopter hub is the primary source of the inaccuracies in drag predictions for design. The flow over a hub is characterized by periodic forcing and vortex interactions in addition to the rotating flow. The flow complexity is augmented due to interactions between the small actuator tubes, wires and linkages used on a typical helicopter hub. Hence a systematic study requires a large range of Reynolds number effects to be taken into account. Prior experimental research of hub drag has been geared towards improving drag characteristics of current hub designs by the addition of fairings. Sikorsky Inc. has explored various fairing designs to reduce flow separation and interference drag between the hub and fuselage.<sup>5</sup> Previous studies have primarily related frontal area of the hub as the primary variable affecting hub drag,<sup>6</sup> consequently the use of fairing on a existing hub design does not resolve the issue. This is especially true for articulated hubs, where a significant volume is required to locate the control hinges. Although there exists empirically correlated analytical estimates to predict hub drag based on frontal area, it has been inconsistent when accounting for interference effects and frontal area.<sup>7</sup> Considerations for hub displacement from the fuselage have been made, weighing the effects of increased frontal area to decreased

---

<sup>\*</sup>AIAA student member, Graduate Research Assistant, Corresponding Author, vrishank@gatech.edu

<sup>†</sup>AIAA student member, Graduate Research Assistant

<sup>‡</sup>AIAA Associate Fellow, Professor

<sup>§</sup>AIAA Associate Fellow, Associate Professor

interference.<sup>6</sup> Bell Helicopter, gathered data on a 1/5 scale helicopter for both an isolated fuselage and a fuselage/hub configuration, with corresponding computational models which predict measured values within 5% when evaluating pitch attitude variations.<sup>8</sup>

A typical hub is constructed from a plethora of bluff bodies, which contribute significantly to the hub drag. Bluff bodies are associated with poor performance characteristics and higher drag. The primary drag component in these bluff bodies is due to flow separation rather than viscous effects. The pressure drag of the bluff bodies results from shed vortices in the wake, affect the performance of both commercial and military air vehicles.<sup>9</sup> While many studies of two-dimensional (2D) bluff bodies have been performed in the past, three-dimensional (3D) studies are typically restricted to spheres and cylinders of varying aspect ratios and/or Reynolds numbers. Reynolds number parametric studies provide a sequence of distinct bifurcations which produce significant and measurable differences in the flowfield.<sup>10</sup> While there have been studies concentrated on the loading of more complex hub configurations,<sup>5,8</sup> there are few studies of the flow topology of the wake behind more complex bodies of revolution. One of these is an investigation by Cannon, who experimentally found two counter rotating helical modes in the wake of bullet shaped bodies.<sup>11</sup>

Previous work conducted at Georgia Tech with a two pronged approach of experimental and computations methods quantified the different sources of hub drag and aimed to tighten the tolerances of empirical upper-bound predictions suitable for conceptual design. In addition, the capability of CFD in contributing to the accurate prediction of drag and wakes to augment experimental studies was evaluated. While prior papers<sup>12,13</sup> have evaluated the drag characteristics of the hub, this work focuses on the hub wake. In order to determine the frequency content of the wake, spectral analysis was conducted on the rotating hub at various locations using hot-wire anemometry and compared to CFD.

## II. Methodology

### A. Experiment

Experiments were conducted in the John J. Harper low speed wind tunnel located at the Daniel Guggenheim School of Aerospace Engineering of Georgia Institute of Technology. A generic four bladed hub model was assembled to approximately one-quarter scale to that of a 10-ton helicopter (Fig. 1). The model includes structures to represent hub plates, blade shanks, a swashplate, pitch links, drive shaft and the required hardware for assembly. Though greatly simplified from the complexities of full-scale hubs with hydraulic lines and intricate mechanisms, this model provides the interference and flow separation attributed to the full-scale system while maintaining the principal geometric characteristics.

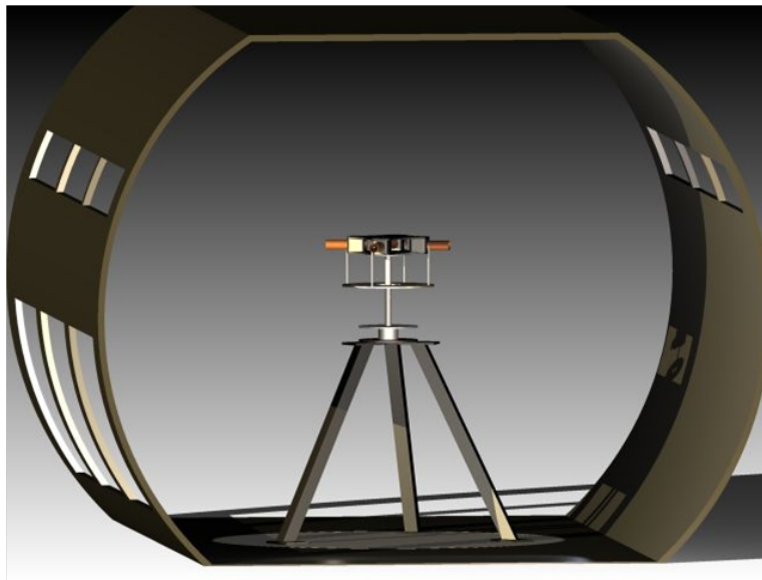


Figure 1. Hub model within John J. Harper wind tunnel test section.

The progression of data acquisition and CFD simulation was initiated with static hub tests. The model

was arranged in various azimuthal orientations throughout a series of runs, always at zero angle of attack. Six-axis force transducer data were obtained for a  $90^\circ$  azimuthal sweep in  $15^\circ$  increments along a range of tunnel speeds. Following static runs, tests were performed on the rotating hub configuration. A range of rotation rates was explored, from 4 to 240 rpm.

In addition, the hub was deconstructed in stages to measure the change in drag which could be attributed to each structural component. Since most theoretical drag prediction methods have been developed for the interference affects between two streamlined bodies, or one streamlined body and one bluff body (for example a wing joint with a fuselage), measuring the interference affects of the hub components was left to experimental trials. Therefore, drag was measured without the contribution of the blade shanks, shanks and hub plates, pitch links and so on until only the hub drive shaft remained. The affect of rotation on the deconstructed model was also measured and is presented here.

In addition to force measurements by an ATI Gamma 6-degree of freedom force transducer, a detailed velocity map of the hub wake was obtained by PIV acquisition. The illumination is provided with a Litron double-pulsed Nd:YAG laser(532 nm, 200mj/pulse) and captured by a LaVision Imager Intense CCD camera (Imager Pro X 2M -  $1600 \times 1200$  pixels, 14 bits). The last experimental measurements were conducted with a single axis hot-wire probe to measure the frequency spectra of velocity fluctuations along the tunnel axis.

## B. Computational Efforts

A computational investigation has been undertaken using FUN3D,<sup>14,15</sup> a NASA developed unstructured solver with overset grid capability. Overset functionality, which is essential to simulate grid motion of a rotating hub in the presence of a non-rotating test facility or fuselage, is achieved via SUGGAR++<sup>16</sup> and DiRTlib.<sup>17</sup> FUN3D's capabilities have been successfully applied to rotorcraft applications of both compressible and incompressible regimes.<sup>18-20</sup> In order to isolate the effects of the overset grid, both the static and rotating simulations employ overset grids, keeping the same initial near-body grid overlaid on a test facility background grid for both static and rotating simulations.

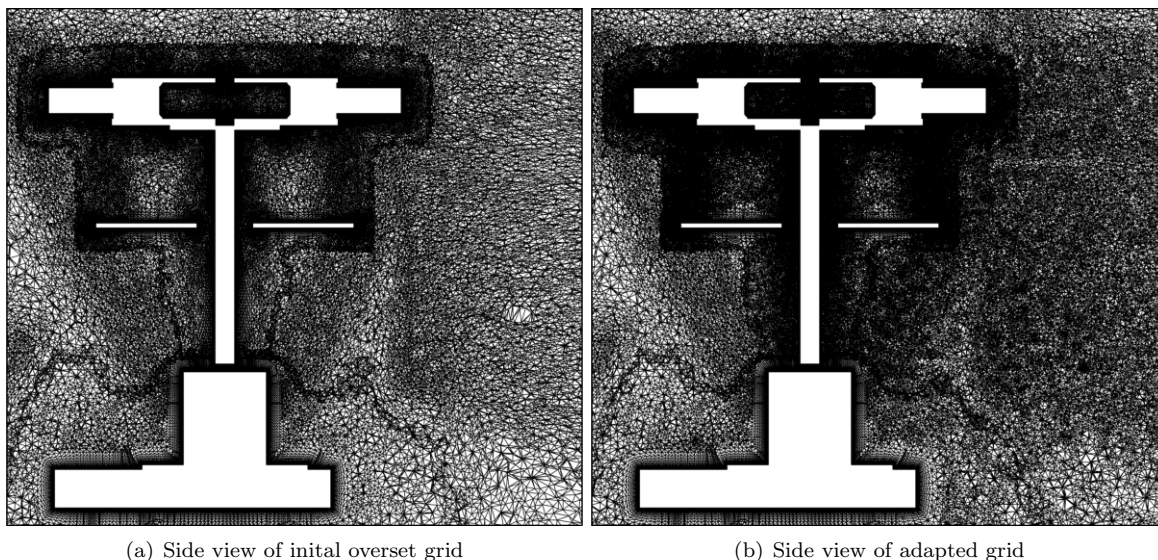


Figure 2. Refinement of the wake region due to grid adaptation.<sup>12</sup>

An overset unstructured grid adaptation capability<sup>21</sup> is utilized (see for example, Fig. 2) in order to minimize numerical dissipation and computational costs due to prohibitively large grid sizes. The time-dependent adaptation metric applied to the present study used the vorticity-magnitude indicator, analogous to the guidelines described by Shenoy et al.<sup>13</sup> A clear advantage of this technique is that grids may be optimized for different flow conditions and geometric orientations without need to manually tailor the grid for a particular problem. It is noted that previous numerical investigations<sup>5,8</sup> of hub drag have not examined the ability of grid adaptation to improve predictions of the loading or the flow features of the unsteady wake.

A hybrid Reynolds-Averaged Navier-Stokes (RANS) and large eddy simulation (LES) turbulence approach (GT-HRLES)<sup>22</sup> was used to obtain time-accurate evaluations of the unsteady hub wake. This hybrid formulation blends the  $k - \omega$  SST RANS model with a one-equation LES model for the subgrid-scale turbulence kinetic energy  $k^{sgs}$ . The dimensional time step (0.3472 milliseconds) was selected equivalent to a  $0.5^\circ$  azimuthal sweep of the 240 rpm rotating hub and is applied to all the cases studied. Each time step was augmented with as many as 40 Newton sub-iterations to increase the temporal accuracy of the simulation. A temporal error controller maintained a specific residual error so that the number of sub-iterations at each time step will varied, but an overall drop in the residual magnitude of 2 orders ensured that 2nd order time accuracy was maintained.<sup>23</sup>

A baseline overset grid of 11.1 million nodes was adapted using vorticity magnitude as the adaptation indicator. Depending on the flow conditions and configuration, the adapted grid sizes varied as described in Table 1. The background grid included the wind tunnel test section, where walls were modeled as inviscid surfaces. The hub geometry, illustrated in Fig. 3, included the details of the experimental model, such as pitch links and associated hardware, which have been shown to influence the hub drag.<sup>13</sup>

	Initial Grid	Adapted
Static hub at $0^\circ$ orientation ( $U_\infty = 30mph$ )	11.1 M nodes	20.9 M nodes
Rotating hub at 240 rpm ( $U_\infty = 30mph$ )	11.1 M nodes	29.0 M nodes
Rotating hub at 240 rpm ( $U_\infty = 50mph$ )	11.1 M nodes	28.9 M nodes

**Table 1. Effect of grid adaptation on the grid size.**

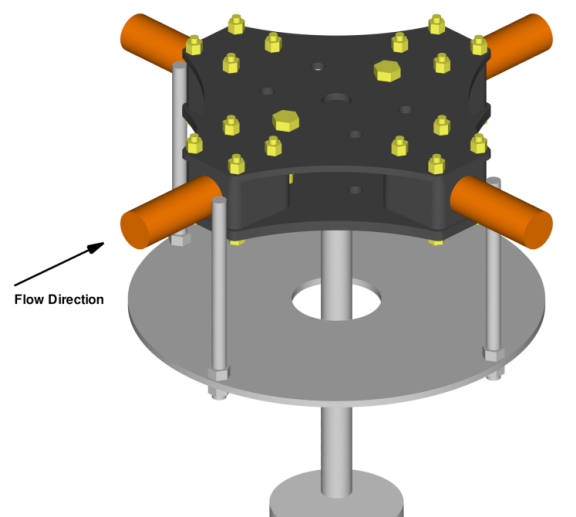


**Figure 3. Hub geometry used for CFD simulations.**

In order to ascertain the ability of the CFD to capture the details of the wake, studies were performed to establish convergence of both the time step selection as well as the number of adaptation iterations. The power spectral density (PSD) plots of velocity fluctuations at a point half a diameter downstream are presented in Fig. 4. Since good comparison was achieved in the spectral power amplitude between the current and a coarser time step ( $\Delta t = 0.3472$  ms and  $\Delta t = 0.6944$  ms, respectively), time step convergence was established.

Shenoy et al.<sup>13</sup> examined the effect of grid adaptation on the drag of the hub as noted in Table 2. Grid independence with respect to drag is ascertained after the first adaptation cycle since the difference in drag from the second adaptation iteration yielded less than 1% difference, while with the first adaptation iteration, drag refinement was as much as 16%. Further adaptations were deemed impractical for the practicing engineer given that grid size may increase by as much as 50% with each adaptation cycle.

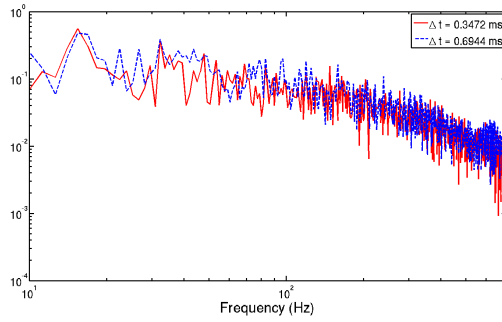


Figure 4. Normalized PSD of velocity fluctuations in the hub wake for the rotating hub at 240 rpm at 30 mph.

Table 2. Effect of adaptation on drag prediction.<sup>13</sup>

Adaptation Iteration	1	2
Static hub at 0° orientation	+3.3%	-0.47%
Static hub at 45° orientation	+15.8%	+0.77%

### III. Results

Results are presented in a progression from integrated loads to flowfield detail to frequency spectra. Both experimental and computational results are used for analysis. The first set of evaluations is the measurement of integrated drag and side force using experiments and computations, at various levels of assembly. Next, the effects of rotation were determined. The flow velocity field is also examined using both experimental and computational data.

#### A. Static and Dynamic Force Measurement

The drag obtained from the static, rotating, and deconstructed configurations for a range of wind tunnel speeds is plotted in Figure 5. Several configurations are shown together to highlight the many qualities of the drag contributions.

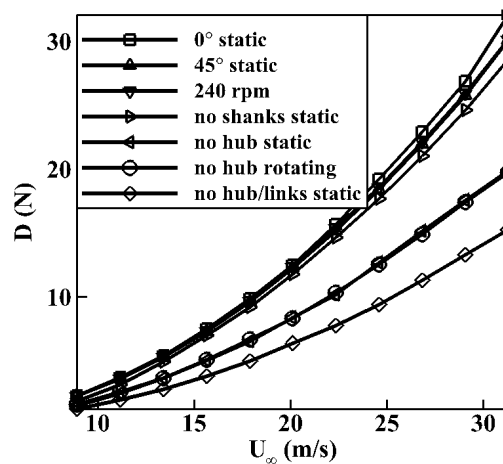


Figure 5. Variation of the experimentally measured hub drag with azimuth and free stream velocity.<sup>12</sup>

First, it can be observed that drag is a maximum for the static hub when it is oriented at  $0^\circ$  azimuth (blade shanks normal and perpendicular to the free stream), corresponding to the orientation of maximum the hub front area. Nearly the same drag is obtained for both the  $45^\circ$  static orientation and the rotating hub at 240 rpm, which is not unexpected since the  $45^\circ$  orientation is representative of the average frontal area of the rotating hub. This result is in agreement with previous findings of an investigation performed by Sheehy and Clark for unfaired hubs.<sup>7</sup>

Examination of CFD surface pressure coefficient distribution (Fig. 6) highlights the differences between the  $0^\circ$  static orientation and the rotating hub at 240 rpm. While some features of the pressure distribution are retained, significant pressure decrease (increase in suction peak) can be observed on the advancing side (left side of figure) and the retreating side of the hub (right side of figure). Further details of these analyses can be found in Ortega et al.<sup>12</sup>

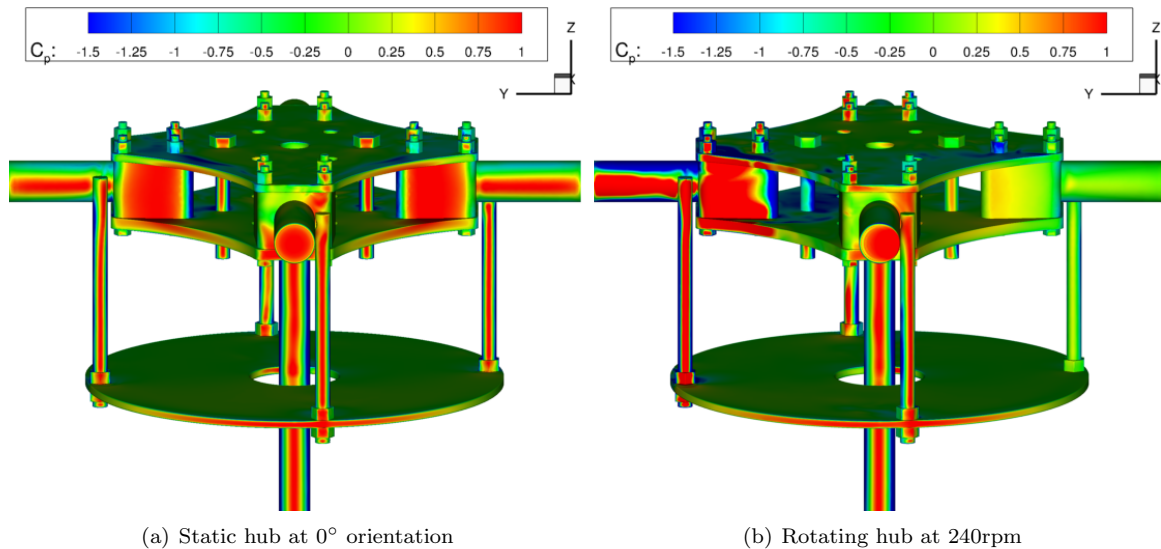


Figure 6. Comparison of surface pressure distributions obtained from CFD.<sup>12</sup>

Figure 7 shows little variation of drag normalized by the free stream dynamic pressure over the range of forward flight speeds. Slight Reynolds number dependence is observed for the complete model at  $0^\circ$  orientation. The scaling of the vertical axis is amplified for visualization.

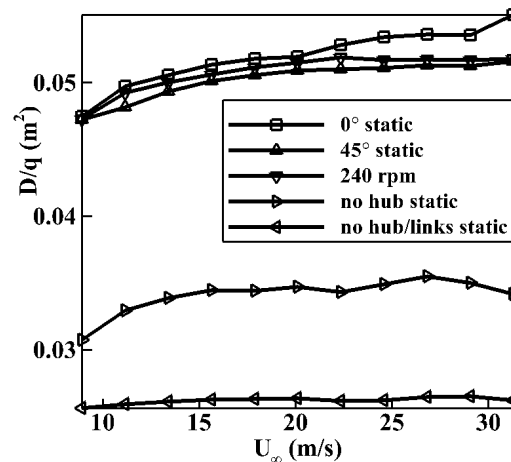


Figure 7. Drag scaled by tunnel dynamic pressure.<sup>12</sup>

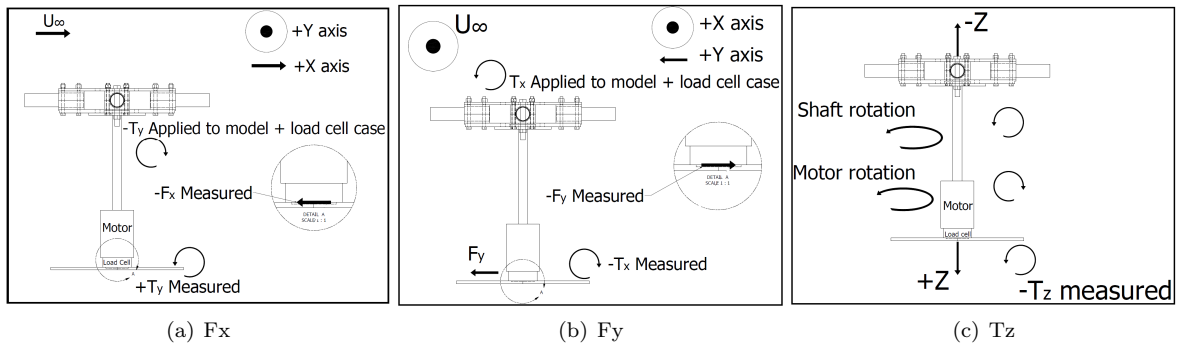


Figure 8. Free body diagrams of loads and moments applied to the hub model and sign validation of measurements read from the force transducer.<sup>12</sup>

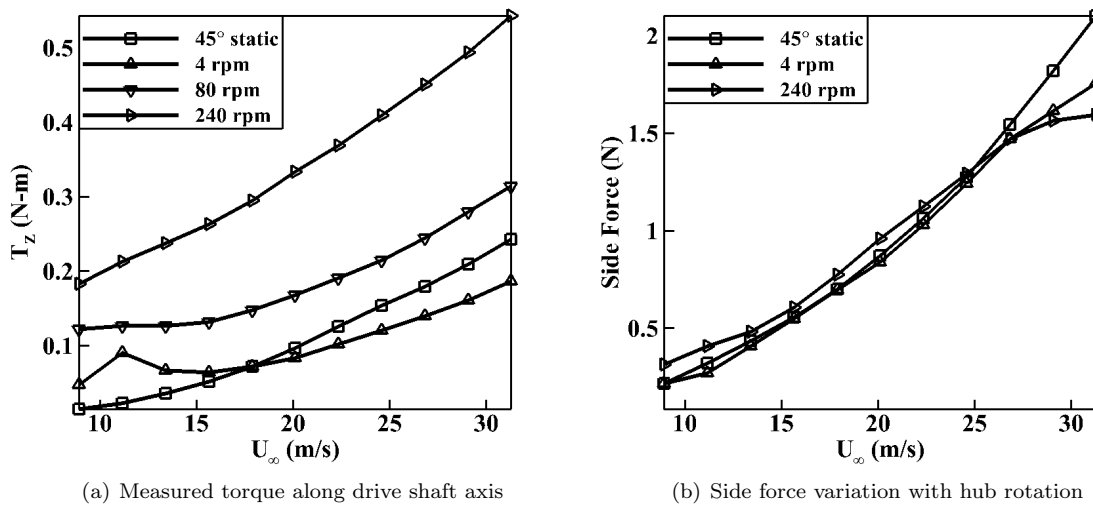


Figure 9. Variation in forces with changing rotational and free stream speeds.<sup>12</sup>

Data acquisition from the rotating model presents the challenge of decoupling the drag component from the anti-torque of the rotating shaft and motor system. The force transducer is situated underneath a compact high torque stepper motor that drives the hub shaft. A free body diagram illustrating the decoupled forces and moments is detailed in Fig. 8. Negligible coupling was found between the measured torque about the shaft axis and the tunnel axis. This was verified by detailed load cell calibration with the mounted hub model as well as comparison of torque measurements with static tests. Torque measurements are shown as positive values in Fig. 9(a) for clarity of trends, however due to the orientation of the force transducer with respect to the model, measured torques along the drive shaft axis were along the negative z-axis of the load cell. Further details can be found in the work by Ortega et al.<sup>12</sup>

## B. Wake Characterization

The unsteady wake of the hub can be characterized through the use of particle image velocimetry (PIV), augmented with CFD. Seeding the flow of a bluff body wake to the appropriate density for PIV limits the range of tunnel speeds which yield fair resolution. By means of atomized oil as a seeding medium, velocity deficits in the wake at a location one-half of the hub diameter (Fig. 10) have been profiled for several model orientations. Figure 12 illustrates the typical variation observed in the wake profile for the hub in two static configurations and one case in rotation. The wake of a rotating hub is observed to shift in accordance to the rotation rate and direction. Also, the free stream region for the rotating case shows an increase in velocity with respect to the tunnel speed setting of 20 mph. The static cases of 0° and 45° show substantial

asymmetry, which is interesting as the only asymmetry in the model arises from the pitch link joint with the blade shanks.

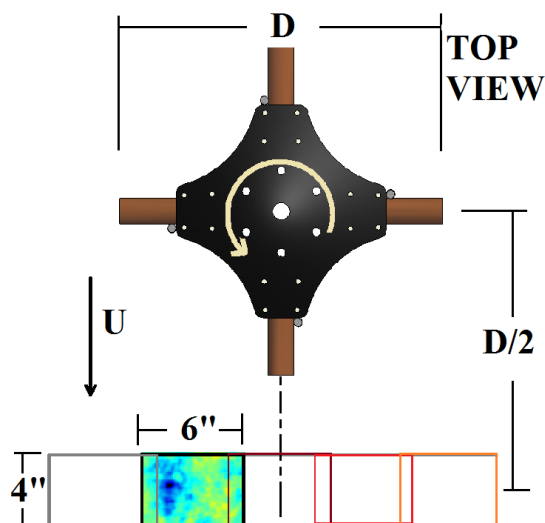


Figure 10. Map of PIV data collection plane comprised of overlapping stitches.<sup>12</sup>

Experimental data were correlated with CFD predictions at the PIV location (Fig. 10) to ascertain the ability of the CFD adapted mesh to capture the details of the wake. Both experimental and computational methods show a contraction of the momentum deficit in the hub wake when the model is oriented at  $45^\circ$  azimuth, corresponding to a reduction of hub drag based on frontal area. The experimental and computational wake velocity deficits correlated very well, as illustrated by Fig. 11. These results provide implications for momentum integral drag resolution via flow computation when overset anisotropic grid adaptation is applied. The causal wake behavior that drive the momentum deficits observed in Fig. 11 is clearly illustrated by the CFD velocity contours downstream of the hub (Fig. 12). The largest deficit at the static hub centerline is clearly defined by the strong velocity deficit at the central portion of the hub wake. This region is in the direct wake of the front and aft shank-block assemblies behind the hub. Behind the lower portion of the geometry, the driveshaft and front and aft pitch links contribute to the central wake deficits. There two secondary wake deficits appearing behind the two lateral shank-block assemblies and their associated pitch links. When the hub rotates in a counter clockwise direction, the primary velocity deficit is translated upward and to the right, appearing behind the right (aft looking forward) blade shank. The primary velocity deficit appears to have coalesced with that of the right-side geometry, leveling only a secondary velocity deficit from the left-side, which has also translated in the positive  $y$ -direction (to the right) of the flow induced by the counter clockwise rotation. The shifted wake indicated the presence of the Magnus effect,<sup>24</sup> earlier observed to be an influencing factor in rotating hub evaluations.<sup>13</sup>

### C. Frequency Spectra

A single axis hot-film constant temperature anemometer sensor measured velocity fluctuations in the hub wake. Samples were collected at four locations located half a diameter downstream of the hub center on a plane bisecting the hub, as depicted in Fig. 13. Data was collected for the static hub oriented at  $0^\circ$  as well as the rotating hub (240 rpm). PSD plots of both experiment and CFD for the static and rotating tests at a 30 mph free stream speed are presented in Figs. 14 and 15, correspond to locations moving inboard of the hub wake. The spectra are obtained by applying a correction factor for hot-wire sensitivity suggested by Champagne and Sleicher.<sup>25</sup>

Both experimental sets of PSD show an increase in broadband turbulence as the sensor is placed further inboard. The power spectra plots generally compare well against the  $5/3$  law, characterizing homogeneity of turbulence.<sup>26</sup> A study of the shedding frequencies of bluff bodies by Sakamoto and Arie<sup>27</sup> provides Strouhal numbers of circular cylinders of varying aspect ratios. Their predicted shedding frequencies are in agreement

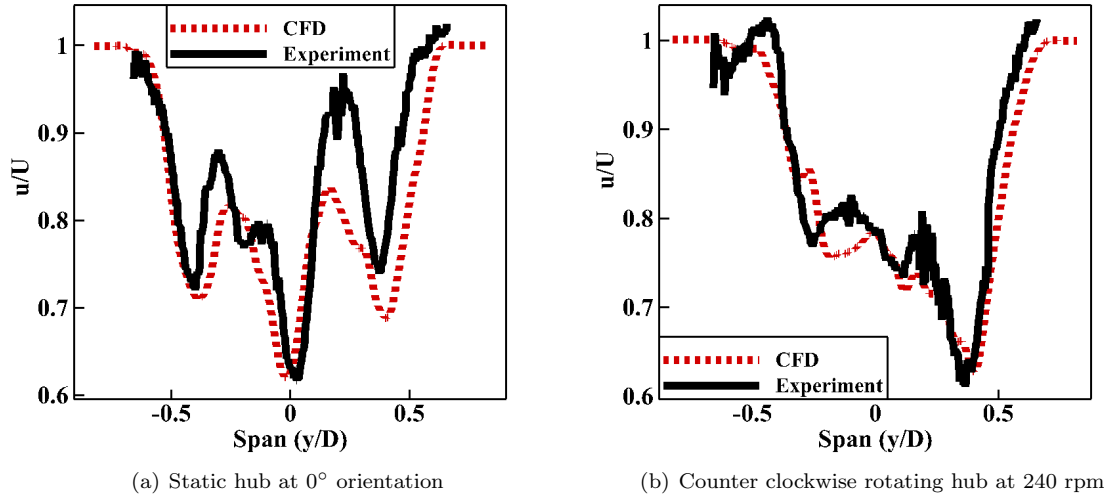


Figure 11. Comparison of PIV and CFD data for the tunnel axis wake velocity deficit.<sup>12</sup>

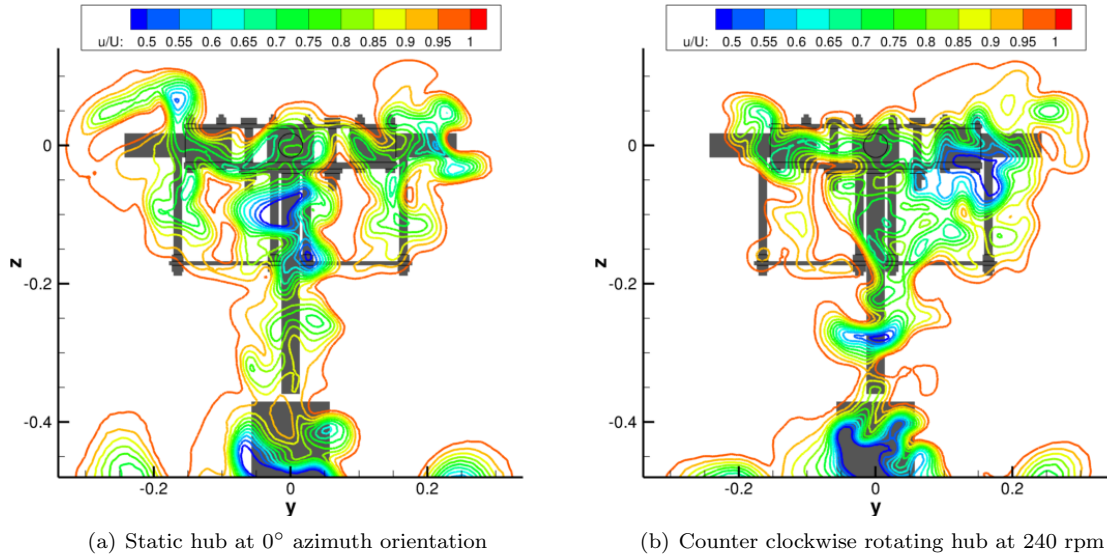


Figure 12. Velocity contours 1 hub diameter downstream of the hub center.<sup>12</sup>

with the blade shank frequency of approximately 50 Hz, observed in locations 2 and 3 of the static test (Fig. 14), just behind the shank. There is a noticeable amplitude spike for all sampling locations of the rotating test case that corresponds to the predicted 4 per revolution signal of the 4-bladed hub model. Both the experimental and CFD efforts capture this 16 Hz frequency as the hub rotates at 240 rpm (4 rev/sec). The next harmonic of this frequency (8 per rev.) is greatly amplified at the inboard sampling location, well within the wake region.

Better agreement with 5/3 law slope is noticed for both the experimental and CFD results at inboard locations. The turbulence displays an expected broad range of scales in the bluff body wake region. To examine the character of the CFD simulation, contours of the HRLES turbulence model's blending function are given in Fig. 16. Values near 1 indicate that the RANS formulation is in effect and values near 0 indicate regions dominated by LES. The four locations show that the flowfield in this region of the wake displays LES behavior, enabling the simulation to capture of the broad range of turbulent scales obtained in the power

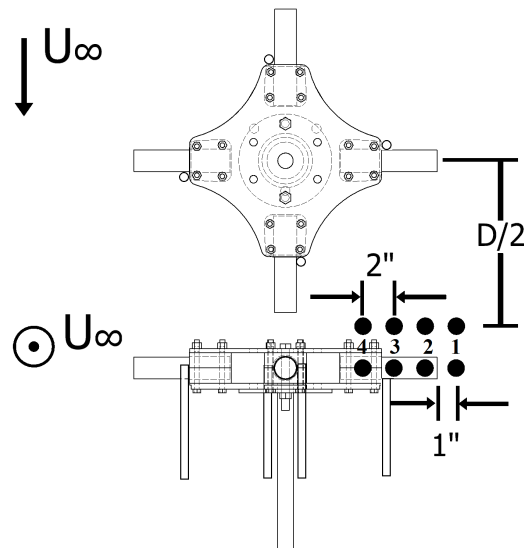


Figure 13. Down stream hot-wire sampling locations. The hub here is oriented at  $0^\circ$ .

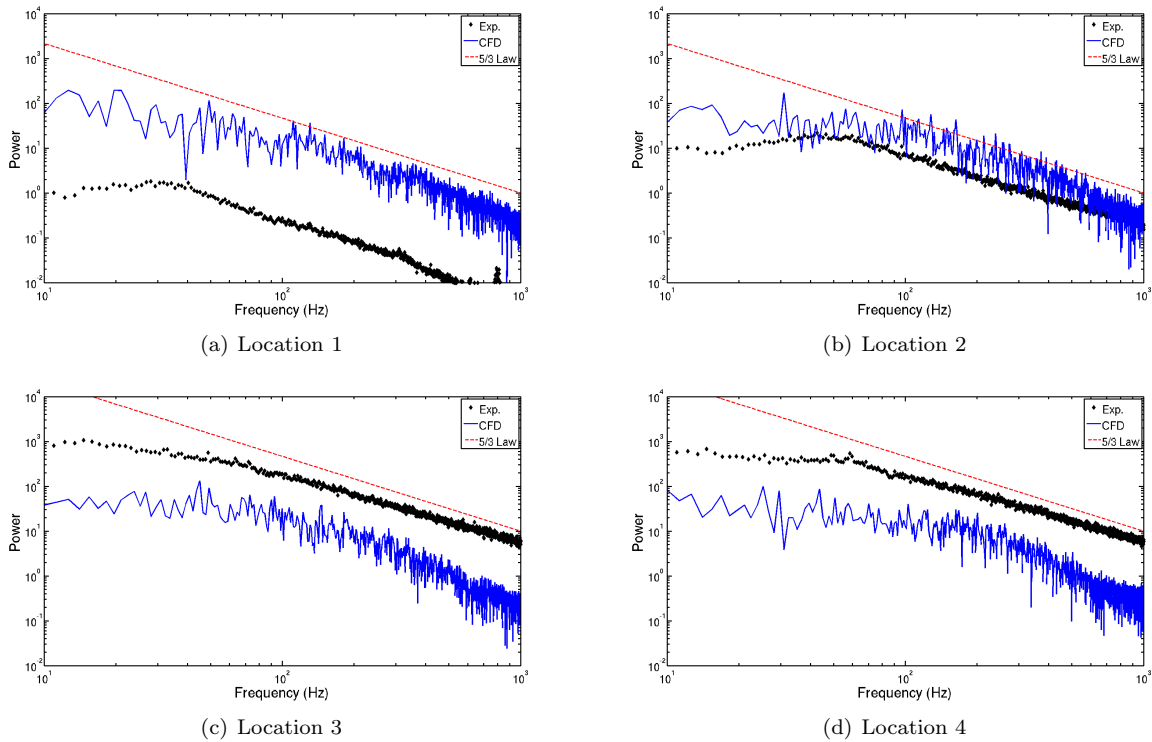
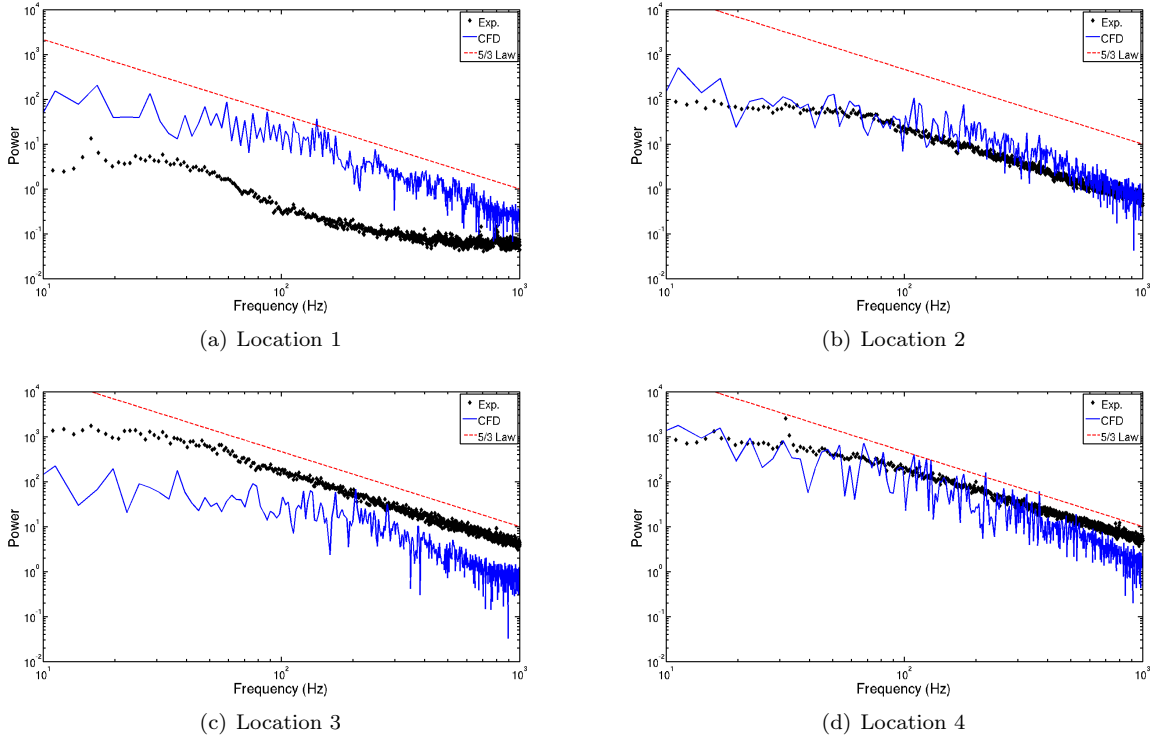


Figure 14. PSD of velocity fluctuations in the hub wake for the static hub at  $0^\circ$  orientation at 30 mph.

spectra.

In addition to the 30 mph free stream results, tests were conducted at 50 mph for the rotating case at 240 rpm. The resulting power spectra is plotted in Fig. 17. Due to greater the energy of the mean flow, the power amplitudes increase in comparison to that obtained from the 30 mph free stream case. However, the spectral features from both the free stream speeds are in general agreement with each other. These include the 4 per rev. and 8 per rev. peaks and the increasing power magnitude and range of turbulent scales at



**Figure 15. PSD of velocity fluctuations in the hub wake for the rotating hub at 240 rpm at 30 mph.**

the inboard locations.

The PSD plots (Figs. 14, 15, and 17) show some disagreement in the magnitude of power obtained between experiment and CFD. The general observation is an over-prediction in power obtained by CFD at location 1. Examination of the wake features in this region (Fig. 18) indicates that the CFD shear layer prediction coincides with location 1, indicating a larger extent of the wake region than that observed in the experiment. This is further substantiated by the wake velocity profiles in Fig. 11, where the extent of the CFD wake is greater in the positive  $y$  side – the region where power spectra are compared. Location 1 corresponds to the spanwise distance  $y/D = 0.55$ , where the velocity magnitude of both the static and rotating cases (Fig. 11 (a) and (b), respectively) appear shifted. In the static test case, the profile shift is noted for a significant portion of the wake. However, the improved velocity correlation for the rotating test case at the inboard locations concur with the turbulence levels that show more accurate agreement. Further, there may be local spatial shifts in features detected indicating that the adaptation methodology may need to be locally enhanced in order to propagate wake features more accurately. Additional experiments may be warranted to test the accuracy of these improvements.

## IV. Conclusions

Experimental and computational efforts have been utilized to obtain the character of the integrated loads and complex wake flowfield of a scaled helicopter main rotor hub. The investigation here and in prior publications<sup>12,13</sup> has yielded these conclusions:

1. Large regions of separated flow contribute to considerable drag from the complex hub. The azimuthal variation of the static hub model shows variation in drag corresponding to the projected frontal area of the hub. For the four-bladed hub configuration, the  $45^\circ$  azimuthal orientation yields nearly identical drag measurements to the mean values obtained for the rotating hub.
2. Side force and torque are present for the static model due to small axial asymmetries in the assembly such as pitch links offset from the shank axes. For both static and rotating cases, the side force

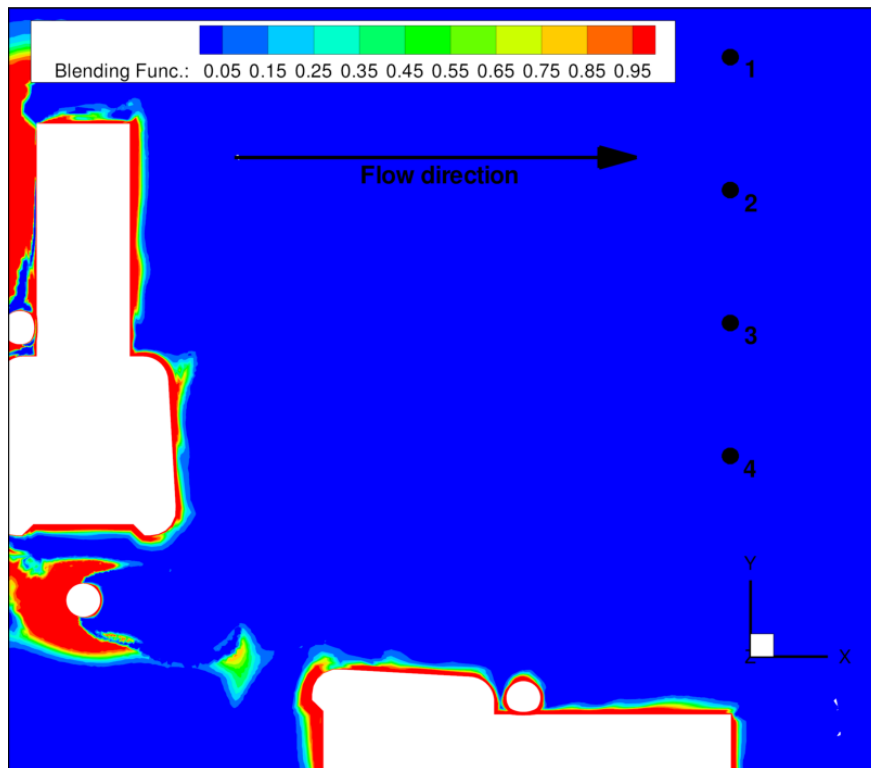
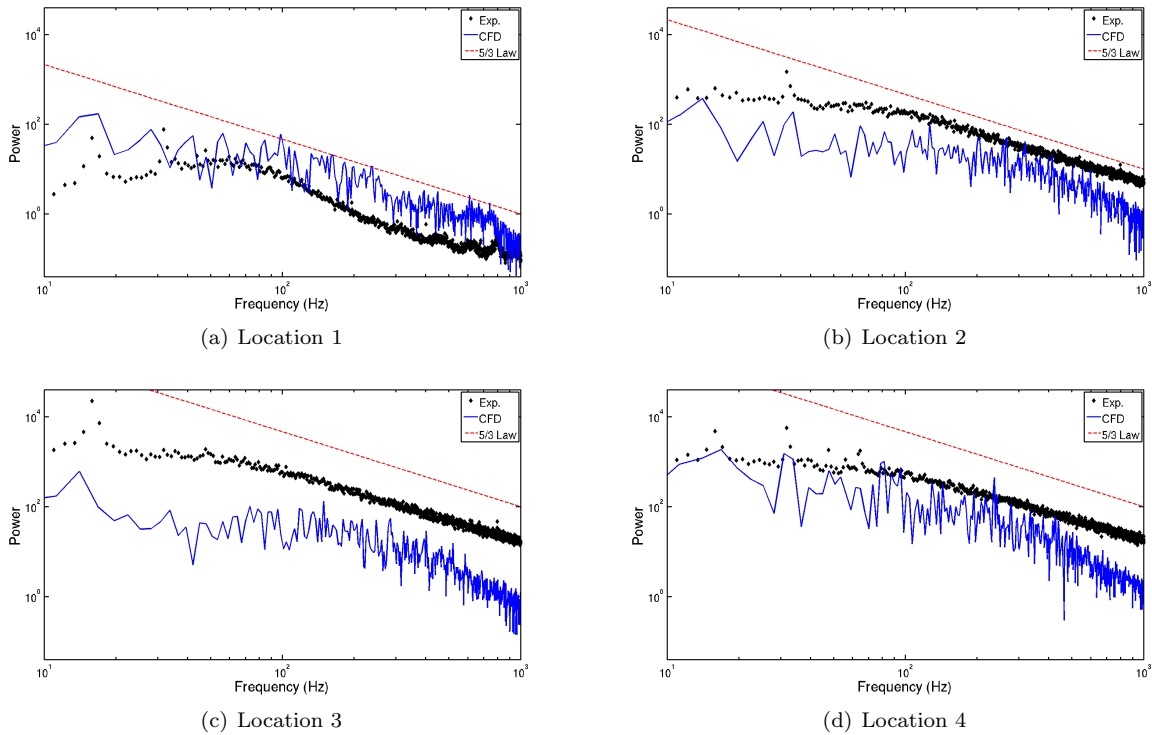


Figure 16. Top view of HRLES blending function contours.

is approximately 1/15 the magnitude of the drag. The use of a 6-axis force transducer has shown sufficient accuracy and the ability to capture the anti-torque contribution of the rotating hub shaft while providing decoupled drag and side force measurements.

3. The resolution of PIV in the hub wake has proven sufficient to detect sideward shifts in the wake velocity deficit due to hub rotation. Variations in the static hub model orientation have also been captured by PIV in the wake field, with asymmetry attributed to the pitch link to blade shank interaction. This is reinforced by the pressure coefficient distribution of the pitch link and blade shanks simulated via CFD. The resolution of drag from components appears to be feasible using wake velocity field results, which is reinforced via excellent correlation between the experimental and CFD results.
4. Computational prediction at the fidelity level of the FUN3D Navier Stokes solver is invaluable tool to augment experimental analyses for this complex hub configuration. Strong correlations between CFD and experimental wake data permit the utilization of the flowfield characteristics predicted by CFD to further explain and clarify the causal physics due to the complex hub geometry.
5. New CFD capabilities developed to permit unstructured overset anisotropic feature-based adaptation across both background and near-body grids are essential to capture the correct physics of complex configurations where significant wake interactions occur in both the near- and far-field grids. Enhancements to adaptation methodology are under way in order to further refine the shifts seen in wake power spectra.
6. The application of the newly developed feature-based overset grid adaptation is beneficial not only for the accurate prediction of the time-averaged wake velocity profiles but also in order to capture the turbulent content of the flow. The methodology complements the HRLES turbulence model which enables a physics-based modelling of small scale features.
7. Turbulence spectra indicate the presence of broadband turbulence in the wake. Correlation with the 5/3 law is observed at the inboard wake locations, indicating locally homogeneous turbulent behavior.



**Figure 17. Power density spectrum of velocity fluctuations in the hub wake for the rotating hub at 240 rpm at 50 mph.**

The rotating spectra shows the presence of strong and energizing 4 per rev. and 8 per rev. frequency content, which are absent in the static spectra. Increasing the free stream speed increases the amplitude of the resultant spectra at all wake locations.

## Acknowledgments

The authors gratefully acknowledge the support of the Office of Naval Research and the associated technical monitor, Dr. Judah Milgram. Assistance from Alex Forbes, Ryan McGowan and Rafael Lozano for the experimental data acquisition and reduction and from Marlin Holmes for the CFD data reduction is acknowledged and greatly appreciated by the authors.

## References

- <sup>1</sup>Williams, R. and Montana, P., "A Comprehensive Plan for Helicopter Drag Reduction," *Proceedings of the American Helicopter Society Symposium on Helicopter Aerodynamic Efficiency*, Hartford, Connecticut, March 6-7, 1975.
- <sup>2</sup>Keys, C. and Wiesner, R., "Guidelines for Reducing Helicopter Parasite Drag," *Journal of the American Helicopter Society*, Vol. 20, 1975, pp. 31-41.
- <sup>3</sup>Hoffman, J., "The Relationship Between Rotorcraft Drag and Stability and Control," *Proceedings of the 31st Annual National Forum of the American Helicopter Society*, Washington, D.C., May 13-15, 1975.
- <sup>4</sup>Kerr, A., "Effect of Helicopter Drag Reduction on Rotor Dynamic Loads and Blade Life," *Proceedings of the American Helicopter Society Symposium on Helicopter Aerodynamic Efficiency*, Hartford, Connecticut, March 6-7, 1975.
- <sup>5</sup>Wake, B., Hagen, E., Ochs, S., and Matalanis, C., "Assessment of Helicopter Hub Drag Prediction with an Unstructured Flow Solver," *Proceedings of the 65th Annual Forum of the American Helicopter Society*, Grapevine, Texas, May 27-29, 2009.
- <sup>6</sup>Sheehy, T. and Clark, D., "A Method for Predicting Helicopter Hub Drag," Tech. Rep. USAAMRDL-TR-75-48, United Technologies Corp., Sikorsky Aircraft Div., January 1976.
- <sup>7</sup>Sheehy, T. and Clark, D., "A General Review of Helicopter Rotor Hub Drag Data," *Journal of the American Helicopter Society*, Vol. 22, No. 2, 1977, pp. 2-11.
- <sup>8</sup>Bridgeman, J. and Lancaster, G., "Physics-Based Analysis Methodology for Hub Drag Prediction," *Proceedings of the*

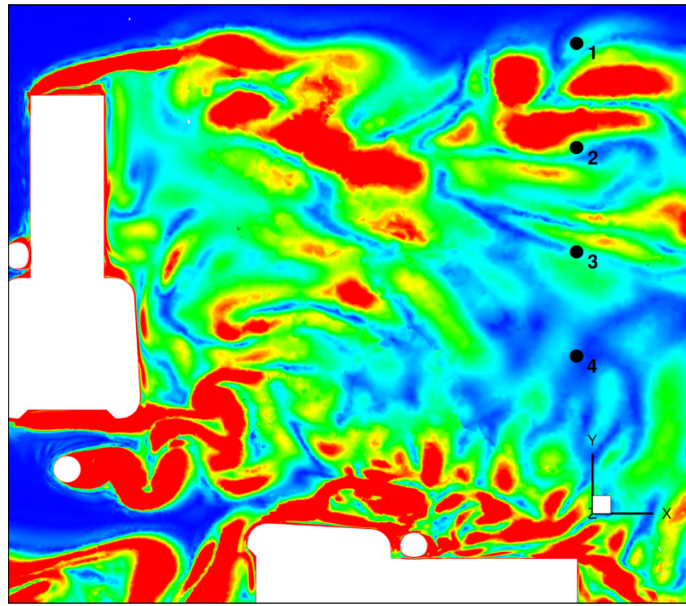


Figure 18. Top view of vorticity contours for the static hub ( $U_\infty = 30\text{mph}$ ).

66th Annual Forum of the American Helicopter Society, Phoenix, Arizona, May 11-13, 2010.

<sup>9</sup>Gregory, J., Porter, C., Sherman, D., and McLaughlin, T., "Circular Cylinder Wake Control Using Spatially Distributed Plasma Forcing," *Proceedings of the 4th Flow Control Conference*, AIAA-2008-4198, Seattle, Washington, June 23-26, 2008.

<sup>10</sup>Roshko, A., "Perspectives on bluff body aerodynamics," *Journal of Wind Engineering and Industrial Aerodynamics*, Vol. 49, No. 1-3, 1993, pp. 79-100.

<sup>11</sup>Seidel, J., Siegel, S., Cohen, K., and McLaughlin, T., "Simulations Of Flow Control Of The Wake Behind An Axisymmetric Bluff Body," *Proceedings of the 3rd AIAA Flow Control Conference*, AIAA-2006-3490, San Francisco, CA, June 5-8, 2006.

<sup>12</sup>Ortega, F., Shenoy, R., Raghav, V., Smith, M., and Komerath, N., "Deconstructing Hub Drag," *Proceedings of the 29th AIAA Applied Aerodynamics Conference*, AIAA-2011-3821, Honolulu, Hawaii, June 27-30, 2011.

<sup>13</sup>Shenoy, R., Holmes, M., Smith, M., and Komerath, N., "Computational Investigation of Hub Drag Deconstruction from Model to Full Scale," *Proceedings of the 37th European Rotorcraft Forum*, Milan, Italy, September 13-15, 2011.

<sup>14</sup>Bonhaus, D., *An Upwind Multigrid Method For Solving Viscous Flows On Unstructured Triangular Meshes*, Master's thesis, George Washington University, 1993.

<sup>15</sup>Anderson, W., Rausch, R., and Bonhaus, D., "Implicit/Multigrid Algorithms for Incompressible Turbulent Flows on Unstructured Grids," *Journal of Computational Physics*, Vol. 128, No. 2, 1996.

<sup>16</sup>Noack, R., Boger, D., Kunz, R., and Carrica, P., "SUGGAR++: An Improved General Overset Grid Assembly Capability," *Proceedings of the 19th AIAA Computational Fluid Dynamics Conference*, AIAA-2009-3992, San Antonio, Texas, June 22-25, 2009.

<sup>17</sup>Noack, R., "DiRTlib: A Library to Add an Overset Capability to Your Flow Solver," *Proceedings of the 17th AIAA Computational Fluid Dynamics Conference*, AIAA-2005-5116, Toronto, Ontario, June 6-9, 2005.

<sup>18</sup>Renaud, T., O'Brien, D. M., Smith, M. J., and Potsdam, M., "Evaluation of Isolated Fuselage and Rotor-Fuselage Interaction Using CFD," *Journal of the American Helicopter Society*, Vol. 53, No. 1, 2008, pp. 3-17.

<sup>19</sup>Abras, J. N., *Enhancement of Aeroelastic Rotor Airload Prediction Methods*, Ph.D. thesis, Georgia Institute of Technology, 2009.

<sup>20</sup>Lynch, C. E., *Advanced CFD Methods for Wind Turbine Analysis*, Ph.D. thesis, Georgia Institute of Technology, 2011.

<sup>21</sup>Shenoy, R. and Smith, M., "Unstructured Overset Grid Adaptation for Rotorcraft Aerodynamic Interactions," *Proceedings of the 67th Annual Forum of the American Helicopter Society*, Virginia Beach, Virginia, May 3-5, 2011.

<sup>22</sup>Lynch, C. E. and Smith, M. J., "Hybrid RANS-LES Turbulence Models on Unstructured Grids," *Proceedings of the 38th Fluid Dynamics Conference and Exhibit*, AIAA-2008-3854, Seattle, Washington, June 23-26, 2008.

<sup>23</sup>Liggett, N. and Smith, M., "Temporal Convergence Criteria for Time-Accurate Viscous Simulations of Separated Flows," *Computers and Fluids*, revisions submitted December 2011.

<sup>24</sup>Hoerner, S. F., *Fluid Dynamic Drag*, Sighar Hoerner, 1965.

<sup>25</sup>Champagne, F. and Sleicher, C., "Turbulence measurements with inclined hot-wires," *Journal of Fluid Mechanics*, Vol. 28, 1967, pp. 177-182.

<sup>26</sup>Pope, S., *Turbulent Flows*, Cambridge University Press, 1st ed., 2000.

<sup>27</sup>Sakamoto, H. and Arie, M., "Vortex shedding from a rectangular prism and a circular cylinder placed vertically in a turbulent boundary layer," *Journal of Fluid Mechanics*, Vol. 126, 1983, pp. 147-165.